Sciencexpress Reports

Order of Magnitude Smaller Limit on the Electric Dipole Moment of the Electron

The ACME Collaboration,* J. Baron,[1] W. C. Campbell,[2] D. DeMille,[3]† J. M. Doyle,[1]† G. Gabrielse,[1]† Y. V. Gurevich,[1]‡ P. W. Hess,[1] N. R. Hutzler,[1] E. Kirilov,[3]§ I. Kozyryev,[3]|| B. R. O'Leary,[3] C. D. Panda,[1] M. F. Parsons,[1] E. S. Petrik,[1] B. Spaun,[1] A. C. Vutha,[4] A. D. West[3]

[1]Department of Physics, Harvard University, Cambridge, MA 02138, USA. [2]Department of Physics and Astronomy, University of California, Los Angeles, CA 90095, USA. [3]Department of Physics, Yale University, New Haven, CT 06511, USA. [4]Department of Physics and Astronomy, York University, Toronto, Ontario M3J 1P3, Canada.

*The collaboration consists of all listed authors. There are no additional collaborators.

†Corresponding author. E-mail: acme@physics.harvard.edu (D.D., J.M.D., G.G.)

‡Present address: Department of Physics, Yale University, New Haven, CT 06511, USA.

§Present address: Institut für Experimentalphysik, Universität Innsbruck, A-6020 Innsbruck, Austria.

||Present address: Department of Physics, Harvard University, Cambridge, MA 02138, USA.

The Standard Model (SM) of particle physics is known to be incomplete. Extensions to the SM, such as weak-scale Supersymmetry, posit the existence of new particles and interactions that are asymmetric under time-reversal (T), and nearly always predict a small, yet potentially measurable (10^{-27}-10^{-30} *e* cm) electron electric dipole moment (EDM, d_e). The EDM is an asymmetric charge distribution along the spin ($\vec{S}$) that is also asymmetric under T. Using the polar molecule thorium monoxide (ThO), we measure $d_e = (-2.1 \pm 3.7_{stat} \pm 2.5_{syst}) \times 10^{-29}$ *e* cm. This corresponds to an upper limit of $|d_e| < 8.7 \times 10^{-29}$ *e* cm with 90 percent confidence, an order of magnitude improvement in sensitivity compared to the previous best limit. Our result constrains T-violating physics at the TeV energy scale.

The exceptionally high internal effective electric field ($\mathcal{E}_{\rm eff}$) of heavy neutral atoms and molecules can be used to precisely probe for d_e via the energy shift $U = -\vec{d}_e \cdot \vec{\mathcal{E}}_{\rm eff}$, where $\vec{d}_e = d_e \vec{S}/(\hbar/2)$ and $\hbar$ is the reduced Planck constant. Valence electrons travel relativistically near the heavy nucleus, making $\mathcal{E}_{\rm eff}$ up to a million times larger than any static laboratory field (*1*–*3*). The previous best limits on d_e came from experiments with thallium (Tl) atoms (*4*) ($|d_e| < 1.6 \times 10^{-27}$ *e* cm), and ytterbium fluoride (YbF) molecules (*5*, *6*) ($|d_e| < 1.06 \times 10^{-27}$ *e* cm). The latter demonstrated that molecules can be used to suppress the motional electric fields and geometric phases that limited the Tl measurement (*5*) (this suppression is also present in certain atoms (*7*)). Insofar as polar molecules can be fully polarized in laboratory-scale electric fields ($\mathcal{E}$), $\mathcal{E}_{\rm eff}$ can be much greater than in atoms. The $^3\Delta_1$ electronic state in the molecule ThO provides an $\mathcal{E}_{\rm eff} \approx 84$ GV/cm, larger than those previously used in EDM measurements (*8*, *9*). Its unusually small magnetic moment reduces its sensitivity to spurious magnetic fields (*10*, *11*). Improved systematic error rejection is possible because internal state selection allows the reversal of $\mathcal{E}_{\rm eff}$ with no change in $\vec{\mathcal{E}}$ (*12*, *13*).

To measure d_e we perform a spin precession measurement (*10*, *14*, *15*) on pulses of $^{232}Th^{16}O$ molecules from a cryogenic buffer gas beam source (*16*–*18*). The pulses pass between parallel plates that generate a laboratory electric field $\mathcal{E}_z\hat{z}$ (Fig. 1A). A coherent superposition of two spin states, corresponding to a spin aligned in the *xy* plane, is prepared using optical pumping and state preparation lasers. Parallel electric ($\vec{\mathcal{E}}$) and magnetic ($\vec{\mathcal{B}}$) fields exert torques on the electric and magnetic dipole moments, causing the spin vector to precess in the *xy* plane. The precession angle is measured with a readout laser and fluorescence detection. A change in this angle as $\vec{\mathcal{E}}_{\rm eff}$ is reversed is proportional to d_e.

In more detail, a 943 nm laser beam optically pumps molecules from the ground electronic state into the lowest rotational level, $J = 1$, of the metastable (lifetime ~ 2 ms) electronic $H^3\Delta_1$ state manifold (Fig. 1B), in an incoherent mixture of the $\tilde{\mathcal{N}} = \pm 1$, $M = \pm 1$ states. M is the angular momentum projection along the $\hat{z}$ axis. $\tilde{\mathcal{N}}$ refers to the internuclear axis, $\hat{n}$, aligned (+1) or anti-aligned (–1) with respect to $\vec{\mathcal{E}}$, when $|\vec{\mathcal{E}}| > \sim 1$ V/cm (*11*). The linearly polarized state-preparation laser's frequency is resonant with the $H \rightarrow C$ transition at 1090 nm (Fig. 1B). Within the short-lived (500 ns) electronic C state there are two opposite parity $\tilde{\mathcal{P}} = \pm 1$ states with $J = 1$, $M = 0$. For a given spin precession measurement, the laser frequency determines the $\tilde{\mathcal{N}}, \tilde{\mathcal{P}}$ states that are addressed. This laser optically pumps the bright superposition of the two resonant $M = \pm 1$ sublevels out of the H state, leaving behind the orthogonal dark superposition that cannot absorb the laser light; we use this dark state as our initial state (*19*). If the state preparation laser were polarized along $\hat{x}$, the prepared state, $|\psi(\tau = 0), \tilde{\mathcal{N}}\rangle$, has the electron spin aligned along the $\hat{y}$ axis. The spin then precesses in the *xy* plane by angle ϕ to

$$\left|\psi(\tau), \tilde{\mathcal{N}}\right\rangle = \frac{\left[\exp(-i\phi)\left|M = +1, \tilde{\mathcal{N}}\right\rangle - \exp(+i\phi)\left|M = -1, \tilde{\mathcal{N}}\right\rangle\right]}{\sqrt{2}} \qquad (1)$$

As $\vec{\mathcal{E}}$ and $\vec{\mathcal{B}}$ are aligned along $\hat{z}$, the phase ϕ is determined by $|\mathcal{B}_z| = |\vec{\mathcal{B}} \cdot \hat{z}|$, its sign, $\tilde{\mathcal{B}} = \mathrm{sgn}(\vec{\mathcal{B}} \cdot \hat{z})$, and the electron's EDM, d_e:

$$\phi \approx \frac{-\left(\mu_B g \tilde{\mathcal{B}} |\mathcal{B}_z| + \tilde{\mathcal{N}} \tilde{\mathcal{E}} d_e \mathcal{E}_{\rm eff}\right)\tau}{\hbar} \qquad (2)$$

where $\tilde{\mathcal{E}} \equiv \mathrm{sgn}(\vec{\mathcal{E}} \cdot \hat{z})$, τ is the spin precession time, and $\mu_B g$ is the magnetic moment (*15*) of the H, $J = 1$ state where $g = .0044(1)$ and μ_B is the Bohr magneton. The sign of the EDM term, $\tilde{\mathcal{N}}\tilde{\mathcal{E}}$, arises from the relative orientation between $\vec{\mathcal{E}}_{\rm eff}$ and the electron spin, as illustrated in Fig. 1B.

After the spin precesses over a distance of $L \approx 22$ cm ($\tau \approx 1.1$ ms), we measure ϕ by optically pumping on the same $H \rightarrow C$ transition with the state readout laser. The laser polarization alternates between $\hat{X}$ and

$\hat{Y}$ every 5 s and we record the modulated fluorescence signals S_X and S_Y from the decay of C to the ground state (fig. S1A). This procedure amounts to a projective measurement of the spin onto $\hat{X}$ and $\hat{Y}$, which are defined such that $\hat{X}$ is at an angle θ with respect to $\hat{x}$ in the xy plane (Fig. 1A). To normalize out molecule number fluctuations, we compute the asymmetry, (*10*)

$$\mathcal{A} \equiv \frac{S_X - S_Y}{S_X + S_Y} = \mathcal{C}\cos\left[2\left(\phi - \theta\right)\right] \quad (3)$$

where the contrast $\mathcal{C}$ is 94 ± 2% on average. We set $|\mathcal{B}_z|$ and θ such that $\phi - \theta \approx (\pi/4)(2n + 1)$ for integer n, so that the asymmetry is linearly proportional to small changes in φ, and maximally sensitive to the EDM. We measure $\mathcal{C}$ by dithering θ between two nearby values that differ by 0.1 rad, denoted by $\tilde{\theta} = \pm 1$.

We perform this spin precession measurement repeatedly under varying experimental conditions to (a) distinguish the EDM energy shift from background phases and (b) search for and monitor possible systematic errors. Within a "block" of data (fig. S1C) taken over 40 s, we perform measurements of the phase for each experimental state derived from 4 binary switches, listed from fastest (.5 s) to slowest (20 s): the molecule alignment, $\tilde{\mathcal{N}}$; the $\mathcal{E}$-field direction, $\tilde{\mathcal{E}}$; the readout laser polarization dither state, $\tilde{\theta}$; and the $\mathcal{B}$-field direction, $\tilde{\mathcal{B}}$. For each $(\tilde{\mathcal{N}},\tilde{\mathcal{E}},\tilde{\mathcal{B}})$ state of the experiment, we measure $\mathcal{A}$ and $\mathcal{C}$, from which we can extract φ. Within each block, we form "switch-parity components" of the phase, ϕ^u, that are combinations of the measured phases that are odd or even under these switch operations (*13*). We denote the switch-parity of a quantity with a superscript, u, listing the switch labels under which the quantity is odd; it is even under all unlabeled switches. For example, the EDM contributes to a phase component $\phi^{\mathcal{N}\mathcal{E}} = -d_e\mathcal{E}_{\text{eff}}\tau/\hbar$. We extract the mean precession time τ from $\phi^B = -\mu_B g|\mathcal{B}_z|\tau/\hbar$ and compute the frequencies, $\omega^u \equiv \phi^u/\tau$. The EDM value is obtained from $\omega^{\mathcal{N}\mathcal{E}}$ by $d_e = -\hbar\omega^{\mathcal{N}\mathcal{E}}/\mathcal{E}_{\text{eff}}$.

On a slower time scale, we perform additional "superblock" binary switches (fig. S1D) to suppress some known systematic errors and to search for unknown ones. These switches, which occur on the 40-600 s time scales, are: the excited state parity addressed by the state readout lasers, $\tilde{\mathcal{P}}$; a rotation of the readout polarization basis by $\theta \to \theta + \pi/2$, $\tilde{\mathcal{R}}$; a reversal of the leads that supply the electric fields, $\tilde{\mathcal{L}}$; and a global polarization rotation of both the state preparation and readout laser polarizations, $\tilde{\mathcal{G}}$. The $\tilde{\mathcal{P}}$ and $\tilde{\mathcal{R}}$ switches interchange the role of the $\hat{X}$ and $\hat{Y}$ readout beams and hence reject systematic errors associated with small differences in power, shape, or pointing. The two $\tilde{\mathcal{G}}$ state angles are chosen to suppress systematics that couple to unwanted ellipticity imprinted on the polarizations by birefringence in the electric field plates. The $\tilde{\mathcal{L}}$ switch rejects systematics that couple to an offset voltage in the electric field power supplies. We extract the EDM from $\omega^{\mathcal{N}\mathcal{E}}$ after a complete set of the 2^8 block and superblock states. The $\omega^{\mathcal{N}\mathcal{E}}$ is even under all of the superblock switches.

The total dataset consists of ~10^4 blocks of data, taken over the course of ~2 weeks (fig. S1, E and F). During this dataset, we also varied, from fastest (hours) to slowest (a few days): the $\mathcal{B}$-field magnitude, $|\mathcal{B}_z| \approx 1$, 19, 38 mG (corresponding to $|\phi| \approx 0$, π/4, π/2 respectively), the $\mathcal{E}$-field magnitude $|\mathcal{E}_z| \approx 36$, 141 V/cm, and the pointing direction of the lasers, $\hat{k}\cdot\hat{z} = \pm 1$. Figure 2B shows measured EDM values obtained when the dataset is grouped according to the states of $|\mathcal{B}_z|$, $|\mathcal{E}_z|$, $\hat{k}\cdot\hat{z}$, and each superblock switch. All of these measurements are consistent within 2σ.

We compute the 1σ standard error in the mean and use standard Gaussian error propagation to obtain the reported statistical uncertainty. The reported upper limit is computed using the Feldman-Cousins prescription (*20*) applied to a folded normal distribution. To prevent experimental bias, we performed a blind analysis by adding an unknown offset to $\omega^{\mathcal{N}\mathcal{E}}$. The mean, statistical error, systematic shifts, and procedure for calculating the systematic error were determined before unblinding. Figure 2A shows a histogram of EDM measurements. The asymmetry, $\mathcal{A}$, obeys a ratio distribution, which has large non-Gaussian tails in the limit of low signal to noise (*21*). We apply a photon count rate threshold cut so that we only include data with a large signal-to-noise, resulting in a statistical distribution that closely approximates a Gaussian. When the EDM measurements are fit to a constant value, the reduced chi-squared is $\chi^2 = 0.996 \pm 0.006$. Based on the total number of detected photoelectrons (~1000 per pulse) that contribute to the measurement, the statistical uncertainty is 1.15 times that from shot noise (*15*).

To search for possible sources of systematic error, we varied over 40 separate parameters (table S1) and observed their effect on $\omega^{\mathcal{N}\mathcal{E}}$ and many other components of the phase correlated with $\tilde{\mathcal{N}}$, $\tilde{\mathcal{E}}$, or $\tilde{\mathcal{B}}$. These parameters are intentionally applied tunable imperfections, such as transverse magnetic fields or laser detunings. These systematic checks were performed concurrently with the 8 block and superblock switches.

We assume that $\omega^{\mathcal{N}\mathcal{E}}$ depends linearly on each parameter P, so that the possible systematic shift and uncertainty of $\omega^{\mathcal{N}\mathcal{E}}$ is evaluated from the measured slope, $S = \partial\omega^{\mathcal{N}\mathcal{E}}/\partial P$, and the parameter value during normal operation (obtained from auxiliary measurements). If S is not monitored throughout the data set, we do not apply a systematic correction but simply include the measured upper limit in our systematic error budget. Data taken with intentionally applied parameter imperfections is used only for determination of systematic shifts and uncertainties. Table 1 lists all contributions to our systematic error.

We identified two parameters that systematically shift the value of $\omega^{\mathcal{N}}$ within our experimental resolution. Both parameters couple to the AC Stark shift induced by the lasers. The molecules are initially prepared in the dark state with a spin orientation dependent on the laser polarization. If there is a polarization gradient along the molecular beam propagation direction, the molecules acquire a small bright state amplitude. Away from the center of a Gaussian laser profile, the laser can be weak enough that the bright state amplitude is not rapidly pumped away; it acquires a phase relative to the dark state due to their mutual energy splitting, given by the AC Stark shift. An equivalent phase is acquired in the state readout laser. This effect changes the measured phase by $\phi_{AC}(\Delta, \Omega_r) \approx (\alpha\Delta + \beta\Omega_r)$, where Δ, Ω_r are the detuning from and Rabi frequency of the $H \to C$ transition, respectively. The constants α, β are measured directly by varying Δ and Ω_r, and depend on the laser's spatial intensity and polarization profile. These measurements are in good agreement with our analytical and numerical models.

A significant polarization gradient is caused by laser-induced thermal stress birefringence (*22*) in the electric field plates. The laser beams are elongated perpendicular to the molecular beam axis, which creates an asymmetric thermal gradient and defines the axes for the resulting birefringence gradient. By aligning the laser polarization with the birefringence axes, the polarization gradient can be minimized. We have

verified this both with polarimetry (*23*) and through the resulting AC Stark shift systematic (Fig. 3A).

Such AC Stark shift effects can cause a systematic shift in the measurement of $\omega^{\mathcal{N}\mathcal{E}}$ in the presence of an $\tilde{\mathcal{N}}\tilde{\mathcal{E}}$ correlated detuning, $\Delta^{\mathcal{N}\mathcal{E}}$, or Rabi frequency, $\Omega_r^{\mathcal{N}\mathcal{E}}$. We observe both.

The detuning component $\Delta^{\mathcal{N}\mathcal{E}}$ is caused by a non-reversing $\mathcal{E}$-field component $\mathcal{E}^{nr}$, generated by patch potentials and technical voltage offsets, which is small relative to the reversing component, $|\mathcal{E}_z|\tilde{\mathcal{E}}$. The $\mathcal{E}^{nr}$ creates a correlated DC Stark shift with an associated detuning $\Delta^{\mathcal{N}\mathcal{E}} = D\mathcal{E}^{nr}$, where D is the H state electric dipole moment. We measured $\mathcal{E}^{nr}$ via microwave spectroscopy (Fig. 3B), two-photon Raman spectroscopy, and the $\tilde{\mathcal{N}}\tilde{\mathcal{E}}$ -correlated contrast.

The Rabi frequency component $\Omega_r^{\mathcal{N}\mathcal{E}}$, arises from a dependence of Ω_r on the orientation of the molecular axis, $\hat{n} \approx \tilde{\mathcal{N}}\tilde{\mathcal{E}}\hat{z}$, with respect to laser propagation direction, $\hat{k}$. This $\hat{k}\cdot\hat{n}$ dependence can be caused by interference between E1 and M1 transition amplitudes on the $H \rightarrow C$ transition. Measurements of a nonzero $\tilde{\mathcal{N}}\tilde{\mathcal{E}}$ -correlated fluorescence signal $S^{\mathcal{N}\mathcal{E}}$, and an $\tilde{\mathcal{N}}\tilde{\mathcal{E}}\tilde{\mathcal{B}}$ -correlated phase $\phi^{\mathcal{N}\mathcal{E}\mathcal{B}}$, both of which changed sign when we reversed $\hat{k}$, provided evidence for a nonzero $\Omega_r^{\mathcal{N}\mathcal{E}}$. The $\phi^{\mathcal{N}\mathcal{E}\mathcal{B}}$ channel, along with its linear dependence on an artificial $\Omega_r^{\mathcal{N}\mathcal{E}}$ generated by an $\tilde{\mathcal{N}}\tilde{\mathcal{E}}$ correlated laser intensity, allowed us to measure $\Omega_r^{\mathcal{N}\mathcal{E}}/\Omega_r = (-8.0 \pm 0.8)\times 10^{-3}\left(\hat{k}\cdot\hat{z}\right)$, where Ω_r is the uncorrelated (mean) Rabi frequency (see supplementary materials).

By intentionally exaggerating these parameters we verified that both $\mathcal{E}^{nr}$ and $\Omega_r^{\mathcal{N}\mathcal{E}}$ couple to AC Stark shift effects to produce a false EDM. We tuned the laser polarization for each $\tilde{\mathcal{G}}$ state to minimize the magnitude of the systematic slope $\partial\omega^{\mathcal{N}\mathcal{E}}/\partial\mathcal{E}^{nr}$ (Fig. 3A). The correlations $\partial\omega^{\mathcal{N}\mathcal{E}}/\partial\mathcal{E}^{nr}$ and $\partial\omega^{\mathcal{N}\mathcal{E}}/\partial\Omega_r^{\mathcal{N}\mathcal{E}}$ were monitored at regular intervals throughout the data set (fig. S1E). The resulting systematic corrections to $\omega^{\mathcal{N}\mathcal{E}}$ were all < 1 mrad/s.

For a subset of our data, the $\tilde{\mathcal{N}}$ -correlated phase $\phi^{\mathcal{N}}$ was nonzero and drifted with time. We identified the cause of this behavior as an $\tilde{\mathcal{N}}$ -correlated laser pointing $\hat{k}^{\mathcal{N}}\cdot\hat{x} \approx 5$ μrad present in our optical frequency switching setup. We eliminated this effect with improved optical alignment; however, since we were not able to determine the precise mechanism by which $\hat{k}^{\mathcal{N}}$ coupled to $\phi^{\mathcal{N}}$, we chose to include $\phi^{\mathcal{N}}$ variations in our systematic error budget. The slope $\partial\omega^{\mathcal{N}\mathcal{E}}/\partial\phi^{\mathcal{N}}$ (consistent with zero) and the mean value of $\phi^{\mathcal{N}}$ established a systematic uncertainty limit of ~1 mrad/s on $\omega^{\mathcal{N}\mathcal{E}}$.

To be cautious, we include in our systematic error budget possible contributions from the following parameters that caused a nonzero EDM shift in experiments similar to ours: stray $\mathcal{B}$-fields $\mathcal{B}_{x,y,z}^{nr}$ and $\mathcal{B}$-field gradients (*13*); an $\tilde{\mathcal{E}}$ -correlated phase, $\phi^{\mathcal{E}}$, caused by leakage current, $\vec{v}\times\vec{\mathcal{E}}$, and geometric phase effects (*4*); and laser detunings and $\mathcal{E}$-field ground offsets (*5*). We obtained direct $\omega^{\mathcal{N}\mathcal{E}}$ systematic limits of < ~1 mrad/s for each. We simulated the effects that contribute to $\phi^{\mathcal{E}}$ by correlating $\mathcal{B}_z$ with $\tilde{\mathcal{E}}$, which allowed us to place a ~10^{-2} mrad/s limit on their combined effect. Because of our slow molecular beam, relatively small applied $\mathcal{E}$-fields, and small magnetic dipole moment, we do not expect any of these effects to systematically shift $\omega^{\mathcal{N}\mathcal{E}}$ above the 10^{-3} mrad/s level (*10*, *11*).

The result of this first-generation ThO measurement,

$$d_e = \left(-2.1 \pm 3.7_{stat} \pm 2.5_{syst}\right)\times 10^{-29}\ e\ \text{cm} \qquad (4)$$

comes from $d_e = -\hbar\omega^{\mathcal{N}\mathcal{E}}/\mathcal{E}_{eff}$ using $\mathcal{E}_{eff} = 84$ GV/cm (*8*, *9*) and $\omega^{\mathcal{N}\mathcal{E}} = (2.6 \pm 4.8_{stat} \pm 3.2_{syst})$ mrad/s. This sets a 90 percent confidence limit,

$$|d_e| < 8.7\times 10^{-29}\ e\ \text{cm} \qquad (5)$$

that is 12 times smaller than the previous best limit (*4*, *5*), an improvement made possible by the first use of the ThO molecule and of a cryogenic source of cold molecules for this purpose. If we were to take into account the roughly estimated 15 percent uncertainty on the calculated $\mathcal{E}_{eff}$ (*8*), and assume that this represents a 1σ Gaussian distribution width, the d_e limit stated above would increase by about 5 percent. Because paramagnetic molecules are sensitive to multiple T-violating effects (*24*), our measurement should be interpreted as $\hbar\omega^{\mathcal{N}\mathcal{E}} = -d_e\mathcal{E}_{eff} - W_S C_S$, where C_S is a T-violating electron-nucleon coupling, and WS is a molecule-specific constant (*8*, *25*). For the d_e limit above we assume $C_S = 0$. Assuming instead that $d_e = 0$ yields $C_S = (-1.3 \pm 3.0) \times 10^{-9}$, corresponding to a 90 percent confidence limit $|C_S| < 5.9 \times 10^{-9}$ that is 9 times smaller than the previous limit (*26*).

A measurably large EDM requires new mechanisms for T violation, which is equivalent to charge conjugation-parity (CP) violation given the CPT invariance theorem (*2*). Nearly every extension to the SM (*27*, *28*) introduces new CP violating phases ϕ_{CP}. It is difficult to construct mechanisms that systematically suppress ϕ_{CP}, so model builders typically assume $\sin(\phi_{CP}) \sim 1$ (*29*). An EDM arising from new particles at energy Λ in an n-loop Feynman diagram will have size

$$\frac{d_e}{e} \sim \kappa\left(\frac{\alpha_{eff}}{4\pi}\right)^n\left(\frac{m_e c^2}{\Lambda^2}\right)\sin\left(\phi_{CP}\right)\left(\hbar c\right)^{-1} \qquad (6)$$

where α_{eff} (about 4/137 for electroweak interactions) encodes the strength with which the electron couples to the new particles, m_e is the electron mass, and κ ~ 0.1-1 is a dimensionless prefactor (*2*, *30*, *31*). In models where 1- or 2-loop diagrams produce d_e, our result typically sets a bound on CP violation at energy scales Λ ~ 3 TeV or 1 TeV, respectively (*27–29*, *31*). Hence, within the context of many models, our more precise EDM limit constrains CP violation up to energy scales similar to or higher than those explored directly at the Large Hadron Collider.

References and Notes

1. P. G. H. Sandars, The electric dipole moment of an atom. *Phys. Lett.* **14**, 194–196 (1965). doi:10.1016/0031-9163(65)90583-4
2. I. B. Khriplovich, S. K. Lamoreaux, *CP Violation Without Strangeness* (Springer, New York, 1997).
3. E. D. Commins, D. DeMille, in *Lepton Dipole Moments*, B. L. Roberts, W. J. Marciano, Eds. (World Scientific, Singapore, 2010), chap. 14, pp. 519–581.
4. B. Regan, E. Commins, C. Schmidt, D. DeMille, New limit on the electron electric dipole moment. *Phys. Rev. Lett.* **88**, 071805 (2002). doi:10.1103/PhysRevLett.88.071805
5. J. J. Hudson, D. M. Kara, I. J. Smallman, B. E. Sauer, M. R. Tarbutt, E. A. Hinds, Improved measurement of the shape of the electron. *Nature* **473**, 493–496 (2011). doi:10.1038/nature10104 Medline
6. D. M. Kara, I. J. Smallman, J. J. Hudson, B. E. Sauer, M. R. Tarbutt, E. A. Hinds, Measurement of the electron's electric dipole moment using YbF molecules: Methods and data analysis. *New J. Phys.* **14**, 103051 (2012). doi:10.1088/1367-2630/14/10/103051
7. M. A. Player, P. G. H. Sandars, An experiment to search for an electric dipole moment in the $^3P_2$ metastable state of xenon. *J. Phys. B* **3**, 1620–1635 (1970). doi:10.1088/0022-3700/3/12/007
8. L. V. Skripnikov, A. N. Petrov, A. V. Titov, Theoretical study of ThO for the electron electric dipole moment search. *J. Chem. Phys.* **139**, 221103 (2013). doi:10.1063/1.4843955
9. E. R. Meyer, J. L. Bohn, Prospects for an electron electric-dipole moment search in metastable ThO and ThF^+. *Phys. Rev. A* **78**, 010502 (2008). doi:10.1103/PhysRevA.78.010502
10. A. C. Vutha, W. C. Campbell, Y. V. Gurevich, N. R. Hutzler, M. Parsons, D.

Patterson, E. Petrik, B. Spaun, J. M. Doyle, G. Gabrielse, D. DeMille, Search for the electric dipole moment of the electron with thorium monoxide. *J. Phys. B* **43**, 074007 (2010). doi:10.1088/0953-4075/43/7/074007
11. A. C. Vutha, B. Spaun, Y. V. Gurevich, N. R. Hutzler, E. Kirilov, J. M. Doyle, G. Gabrielse, D. DeMille, Magnetic and electric dipole moments of the $H^3\Delta_1$ state in ThO. *Phys. Rev. A* **84**, 034502 (2011). doi:10.1103/PhysRevA.84.034502
12. S. Bickman, P. Hamilton, Y. Jiang, D. DeMille, Preparation and detection of states with simultaneous spin alignment and selectable molecular orientation in PbO. *Phys. Rev. A* **80**, 023418 (2009). doi:10.1103/PhysRevA.80.023418
13. S. Eckel, P. Hamilton, E. Kirilov, H. W. Smith, D. DeMille, Search for the electron electric dipole moment using Ω-doublet levels in PbO. *Phys. Rev. A* **87**, 052130 (2013). doi:10.1103/PhysRevA.87.052130
14. W. C. Campbell *et al*., EPJ Web of Conferences 57, 02004 (2013).
15. E. Kirilov, W. C. Campbell, J. M. Doyle, G. Gabrielse, Y. V. Gurevich, P. W. Hess, N. R. Hutzler, B. R. O'Leary, E. Petrik, B. Spaun, A. C. Vutha, D. DeMille, Shot-noise-limited spin measurements in a pulsed molecular beam. *Phys. Rev. A* **88**, 013844 (2013). doi:10.1103/PhysRevA.88.013844
16. S. E. Maxwell, N. Brahms, R. deCarvalho, D. R. Glenn, J. S. Helton, S. V. Nguyen, D. Patterson, J. Petricka, D. DeMille, J. M. Doyle, High-flux beam source for cold, slow atoms or molecules. *Phys. Rev. Lett.* **95**, 173201 (2005). doi:10.1103/PhysRevLett.95.173201 Medline
17. N. R. Hutzler, M. F. Parsons, Y. V. Gurevich, P. W. Hess, E. Petrik, B. Spaun, A. C. Vutha, D. DeMille, G. Gabrielse, J. M. Doyle, A cryogenic beam of refractory, chemically reactive molecules with expansion cooling. *Phys. Chem. Chem. Phys.* **13**, 18976 (2011). doi:10.1039/c1cp20901a Medline
18. N. R. Hutzler, H.-I. Lu, J. M. Doyle, The buffer gas beam: An intense, cold, and slow source for atoms and molecules. *Chem. Rev.* **112**, 4803–4827 (2012). doi:10.1021/cr200362u Medline
19. H. R. Gray, R. M. Whitley, C. R. Stroud Jr., Coherent trapping of atomic populations. *Opt. Lett.* **3**, 218–220 (1978). doi:10.1364/OL.3.000218 Medline
20. G. J. Feldman, R. D. Cousins, Unified approach to the classical statistical analysis of small signals. *Phys. Rev. D* **57**, 3873–3889 (1998). doi:10.1103/PhysRevD.57.3873
21. J. H. Curtiss, On the distribution of the quotient of two chance variables. *Ann. Math. Stat.* **12**, 409–421 (1941). doi:10.1214/aoms/1177731679
22. S. Eisenbach, H. Lotem, SPIE 8th Meeting on Optical Engineering in Israel 1972 (1992).
23. H. G. Berry, G. Gabrielse, A. E. Livingston, Measurement of the Stokes parameters of light. *Appl. Opt.* **16**, 3200–3205 (1977). doi:10.1364/AO.16.003200 Medline
24. M. G. Kozlov, L. N. Labzowsky, Parity violation effects in diatomics. *J. Phys. At. Mol. Opt. Phys.* **28**, 1933–1961 (1995). doi:10.1088/0953-4075/28/10/008
25. V. A. Dzuba, V. V. Flambaum, C. Harabati, Relations between matrix elements of different weak interactions and interpretation of the parity-nonconserving and electron electric-dipole-moment measurements in atoms and molecules. *Phys. Rev. A* **84**, 052108 (2011). doi:10.1103/PhysRevA.84.052108
26. W. C. Griffith, M. D. Swallows, T. H. Loftus, M. V. Romalis, B. R. Heckel, E. N. Fortson, Improved limit on the permanent electric dipole moment of ^{199}Hg. *Phys. Rev. Lett.* **102**, 101601 (2009). doi:10.1103/PhysRevLett.102.101601 Medline
27. S. Barr, A review of CP violation in atoms. *Int. J. Mod. Phys. A* **08**, 209–236 (1993). doi:10.1142/S0217751X93000096
28. M. Pospelov, A. Ritz, Electric dipole moments as probes of new physics. *Ann. Phys.* **318**, 119–169 (2005). doi:10.1016/j.aop.2005.04.002
29. J. Engel, M. J. Ramsey-Musolf, U. van Kolck, Electric dipole moments of nucleons, nuclei, and atoms: The Standard Model and beyond. *Prog. Part. Nucl. Phys.* **71**, 21–74 (2013). doi:10.1016/j.ppnp.2013.03.003
30. N. Fortson, P. Sandars, S. Barr, The search for a permanent electric dipole moment. *Phys. Today* **56**, 33 (2003). doi:10.1063/1.1595052
31. W. Bernreuther, M. Suzuki, The electric dipole moment of the electron. *Rev. Mod. Phys.* **63**, 313–340 (1991). doi:10.1103/RevModPhys.63.313
32. R. A. Patten, Michelson interferometer as a remote gauge. *Appl. Opt.* **10**, 2717–2721 (1971). doi:10.1364/AO.10.002717 Medline
33. J. Hall, L.-S. Ma, M. Taubman, B. Tiemann, F.-L. Hong, O. Pfister, Jun Ye, Stabilization and frequency measurement of the I_2-stabilized Nd:YAG laser. *IEEE Trans. Instrum. Meas.* **48**, 583–586 (1999). doi:10.1109/19.769663
34. G. Edvinsson, A. Bornstedt, P. Nylén, *Ark. Phys.* **38**, 193 (1968).
35. G. Edvinsson, A. Lagerqvist, Two new band systems in ThO. *Phys. Scr.* **41**, 316–320 (1990). doi:10.1088/0031-8949/41/3/004
36. J. Paulovič, T. Nakajima, K. Hirao, R. Lindh, P. A. Malmqvist, Relativistic and correlated calculations on the ground and excited states of ThO. *J. Chem. Phys.* **119**, 798 (2003). doi:10.1063/1.1578053

Acknowledgments: This research was supported by NSF and the NIST PMG program. We thank M. Reece and M. Schwartz for discussions, and S. Cotreau, J. MacArthur, and S. Sansone for technical support. P.W. Hess was supported in part by the DOE SCGF program. The authors declare no competing financial interests.

Supplementary Materials

www.sciencemag.org/cgi/content/full/science.1248213/DC1
Materials and Methods
Fig. S1
Table S1
References (*32*–*36*)

7 November 2013; accepted 9 December 2013

Published online 19 December 2013
10.1126/science.1248213

Table 1. Summary of systematic errors. Systematic and statistical errors for $\omega^{\mathcal{N}\mathcal{E}}$, in units of mrad/s. All errors are added in quadrature, and are derived from Gaussian 1σ (68%) confidence intervals. In EDM units, 1.3 mrad/s ≈ 10^{-29} *e* cm.

Parameter	Shift	Uncertainty
$\mathcal{E}^{\mathrm{nr}}$ correction	−0.81	0.66
$\Omega_{\mathrm{r}}^{\mathcal{N}\mathcal{E}}$ correction	−0.03	1.58
$\phi^{\mathcal{E}}$ correlated effects	−0.01	0.01
$\phi^{\mathcal{N}}$ correlation		1.25
Non-reversing $\mathcal{B}$-field ($\mathcal{B}_z^{\mathrm{nr}}$)		0.86
Transverse $\mathcal{B}$ -fields ($\mathcal{B}_x^{\mathrm{nr}}$, $\mathcal{B}_y^{\mathrm{nr}}$)		0.85
$\mathcal{B}$-field gradients		1.24
Prep./read laser detunings		1.31
$\tilde{\mathcal{N}}$ correlated detuning		0.90
$\mathcal{E}$-field ground offset		0.16
Total systematic	−0.85	3.24
Statistical		4.80
Total uncertainty		5.79

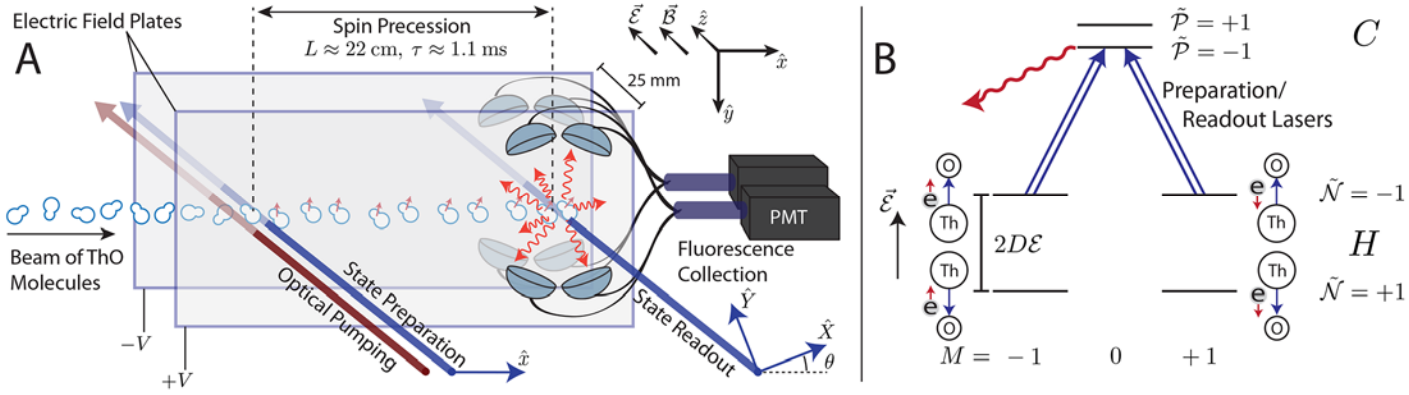

Fig. 1. Schematic of the apparatus and energy level diagram. (**A**) A collimated pulse of ThO molecules enters a magnetically shielded region (not to scale). An aligned spin state (smallest red arrows), prepared via optical pumping, precesses in parallel electric and magnetic fields. The final spin alignment is read out by a laser with rapidly alternating linear polarizations, $\hat{X}$, $\hat{Y}$, with the resulting fluorescence collected and detected with photomultiplier tubes (PMTs). (**B**) The state-preparation and readout lasers (double lined blue arrows) drive one molecule orientation $\tilde{\mathcal{N}} = \pm 1$ (split by $2D\mathcal{E}$ ~ 100 MHz, where *D* is the electric dipole moment of the *H* state) in the *H* state to *C*, with parity $\tilde{\mathcal{P}} = \pm 1$ (split by 50 MHz). Population in the *C* state decays via spontaneous emission, and we detect the resulting fluorescence (red wiggly arrow). *H* state levels are accompanied by cartoons displaying the orientation of $\vec{\mathcal{E}}_{\mathrm{eff}}$ (blue arrows) and the spin of the electron (red arrows) that dominantly contributes to the d_e shift.

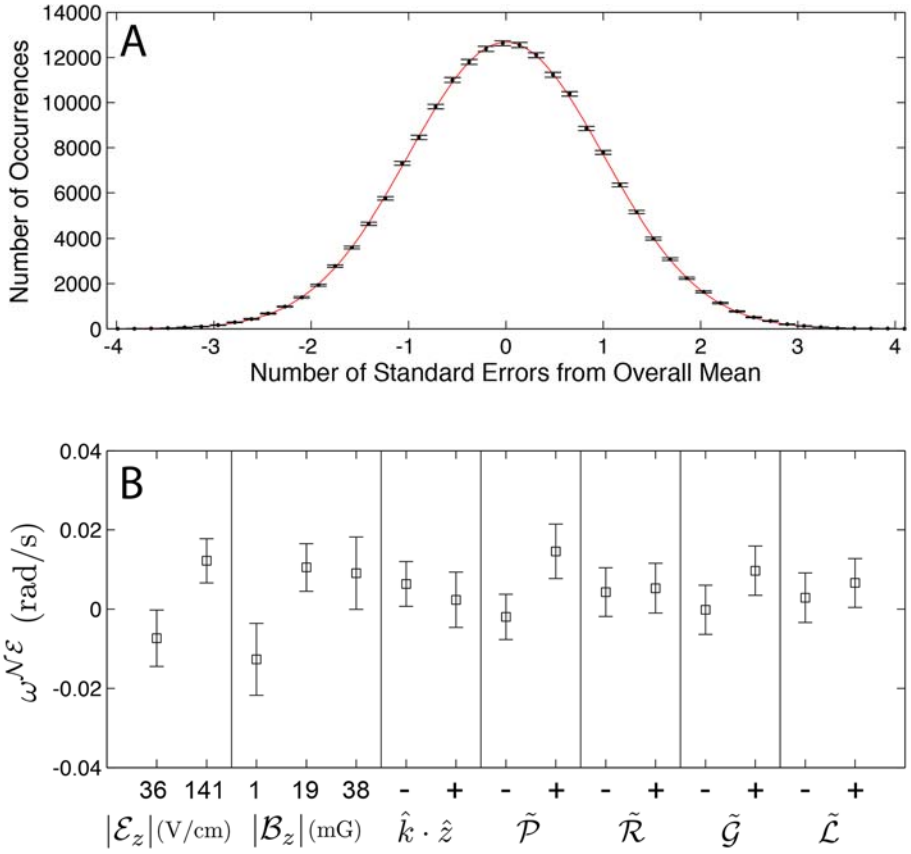

Fig. 2. Statistical spread of $\omega^{\mathcal{N}\mathcal{E}}$ measurements. (**A**) Histogram of $\omega^{\mathcal{N}\mathcal{E}}$ measurements for each time point (within molecule pulse) and for all blocks. Error bars represent expected Poissonian fluctuations in each histogram bin. (**B**) Measured $\omega^{\mathcal{N}\mathcal{E}}$ values grouped by the states of $|\mathcal{B}_z|$, $|\mathcal{E}_z|$, $\hat{k}\cdot\hat{z}$, and each superblock switch, before systematic corrections.

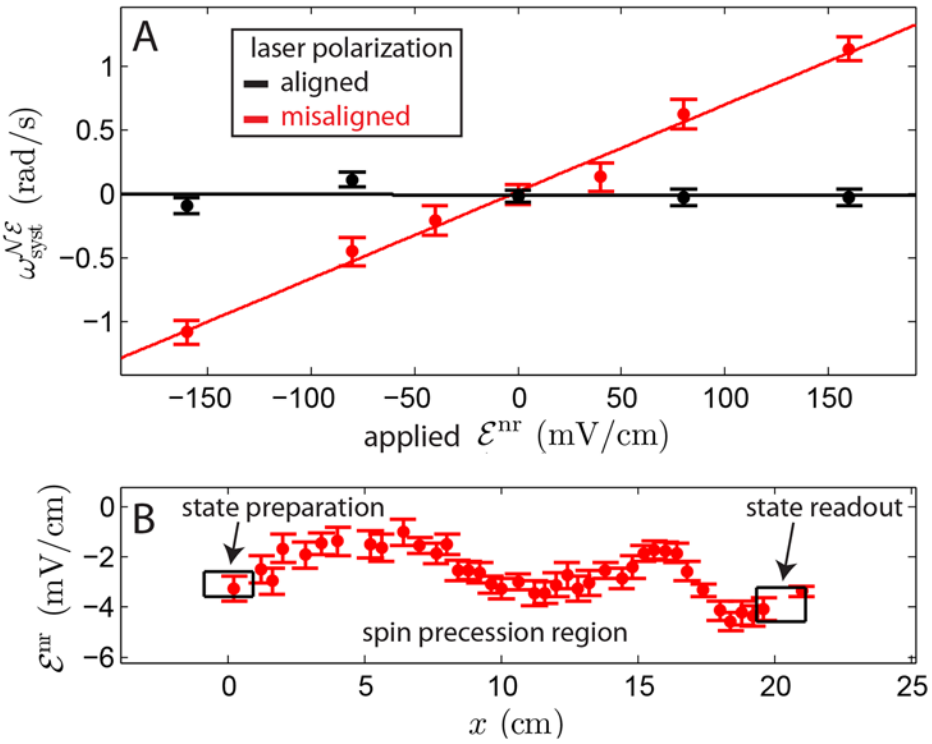

Fig. 3. The $\mathcal{E}^{\mathrm{nr}}$ systematic. (**A**) Tuning out laser polarization gradient and $\partial\omega^{\mathcal{N}\mathcal{E}}/\partial\mathcal{E}^{\mathrm{nr}}$ (see text for details). The red (black) points were taken with the polarization misaligned (aligned) with the birefringence axes of the electric field plates. (**B**) Microwave spectroscopic measurement of $\mathcal{E}^{\mathrm{nr}}$ during normal operation along the molecule beam axis, *x*.